Journal of
Composites Science

MDPI

Article

Highly Sensitive Titanium-Based MXene-Reduced Graphene Oxide Composite for Efficient Electrochemical Detection of Cadmium and Copper Ions in Water

Dharshini Mohanadas [1,2], Rosiah Rohani [1,3,*], Siti Fatimah Abdul Rahman [1], Ebrahim Mahmoudi [1,3] and Yusran Sulaiman [2,4]

[1] Department of Chemical & Process Engineering, Faculty of Engineering and Built Environment, Universiti Kebangsaan Malaysia, UKM, Bangi 43600, Selangor, Malaysia
[2] Department of Chemistry, Faculty of Science, Universiti Putra Malaysia, UPM, Serdang 43400, Selangor, Malaysia
[3] Research Centre for Sustainable Process Technology, Faculty of Engineering & Built Environment, Universiti Kebangsaan Malaysia, UKM, Bangi 43600, Selangor, Malaysia
[4] Functional Nanotechnology Devices Laboratory, Institute of Nanoscience and Nanotechnology (ION2), Universiti Putra Malaysia, UPM, Serdang 43400, Selangor, Malaysia
* Correspondence: rosiah@ukm.edu.my

Abstract: An electrochemically active and promising binary composite that is made up of titanium-based MXene ($Ti_3C_2T_x$) and rGO is developed to simultaneously detect the Cd^{2+} and Cu^{2+}, in water. XRD, FTIR, Raman, XPS, FESEM, elemental mapping, and EDX analysis affirmed the successful formation of the $Ti_3C_2T_x$-rGO composite. The produced $Ti_3C_2T_x$-rGO electrode exhibited a homogeneous rGO sheet covering the $Ti_3C_2T_x$ MXene plates with all the detailed Ti2p, C1s, and O1s XPS peaks. The high-performance $Ti_3C_2T_x$-rGO composite was successfully tested for the Cd^{2+} and Cu^{2+} ions via differential pulse voltammetry (DPV), altering the pH, concentration, and the real water sample's quality. The electrochemical performances revealed that the proposed $Ti_3C_2T_x$-rGO composite depicted excellent detection and quantification limits (LOD and LOQ) for both Cd^{2+} (LOD = 0.31 nM, LOQ = 1.02 nM) and Cu^{2+} (LOD = 0.18 nM, LOQ = 0.62 nM) ions, where the result is highly comparable with the reported literature. The $Ti_3C_2T_x$-rGO was proven highly sensitive towards Cd^{2+} (0.345 $\mu M \mu A^{-1}$) and Cu^{2+} (0.575 $\mu M \mu A^{-1}$) with great repeatability and reproducibility properties. The $Ti_3C_2T_x$-rGO electrode also exhibited excellent stability over four weeks with a retention of 97.86% and 98.01% for Cd^{2+} and Cu^{2+}, respectively. This simple modification of $Ti_3C_2T_x$ with rGO can potentially be advantageous in the development of highly sensitive electrochemical sensors for the simultaneous detection of heavy metal ions.

Keywords: titanium-based MXene; graphene; electrochemical analysis; electrochemical sensor; heavy metal detection

Academic Editor: Jacob Aboudi

Received: 27 March 2025
Revised: 15 April 2025
Accepted: 16 April 2025
Published: 4 May 2025

Citation: Mohanadas, D.; Rohani, R.; Abdul Rahman, S.F.; Mahmoudi, E.; Sulaiman, Y. Highly Sensitive Titanium-Based MXene-Reduced Graphene Oxide Composite for Efficient Electrochemical Detection of Cadmium and Copper Ions in Water. *J. Compos. Sci.* **2025**, *9*, 232. https://doi.org/10.3390/jcs9050232

1. Introduction

"Environmental health hazards" are identified based on the toxicity of the substance and potential exposure to contaminated air, water, soil, and heavy metal ions. They are also classified in the top ten list of the "Agency for Toxic Substances and Disease Registry Priority List of Hazardous Substances" [1]. The most abundant forms of water pollutants that result in negative effects on ecosystems, marine animals, and human health are heavy metals such as copper (Cu), lead (Pb), cadmium (Cd), chromium (Cr), mercury

(Hg), and zinc (Zn). Many detection methods have been invented due to the increasing demand for a better evaluation of the quality of water, specifically in respect to heavy metal contamination. The three distinct types of these heavy metal detection approaches are spectroscopic, electrochemical, and optical detection. In comparison, the electrochemical approach is preferred for identifying heavy metals as it requires quick analytical time, requires cheap and easy-to-operate equipment, has great sensitivity, and possesses excellent selectivity [2,3].

MXene consists of a metal carbide, nitride, or carbonitride nanosheet in a two-dimensional (2D) transition material. Meanwhile, $Ti_3C_2T_x$ is a titanium-based MXene, an extensively developed and explored MXene to be employed in the treatment of water [4]. The $Ti_3C_2T_x$ MXene was developed by researchers for identifying heavy metals, specifically for the detection of Cu^{2+}, Cr^{7+}, Ba^{2+}, and Pb^{2+} utilizing in situ reductions and adsorption techniques. MXene has strong catalytic activity against a variety of water contaminants in a sensing application, in the presence of -O and -OH functional groups, which provide an abundance of active sites for a direct ion exchange process. Shahzad et al. [5] proposed a 2D $Ti_3C_2T_x$ nanosheet that has active interaction with Cu^{2+} ions to produce an adsorption capacity that is 2.7 times larger than that for typically accessible activated carbon. The introduction of $Ti_3C_2T_x$ MXene nanoribbons drastically enhances the adsorption and reduction properties, where promising and simple electrochemical analysis has demonstrated an excellent LOD of 0.94 nM for Cd^{2+} ions [6]. The alkalinized $Ti_3C_2T_x$ ($Ti_3C_2(OH/ONa)_xF_{2-x}$) electrode comprises multiple active Ti-O and Ti-OH sites and has also demonstrated promising signals towards Pb^{2+} purification for environmental remediation [7]. On the other hand, the diverse $Ti_3C_2T_x$ MXene layer has a limited distance within the multiple sheets, which inhibits electrode performance. This is due to only a tiny portion of the electroactive sites being attached during the detection process. Modifying the surface is a viable strategy for improving MXene characteristics for offering potential sensing performance, as this can drastically increase the MXene layer distance. MXene has been altered using numerous electroactive components such as conductive polymers, transition metal oxides, and graphene in order to boost the sensing properties. Xia et al. [8] incorporated carbon black with $Ti_3C_2T_x$ MXene and the result revealed that the aggregation of $Ti_3C_2T_x$ Mxene was successfully prevented, and the electron transfer as well as the electrode surface area had gradually improved via the proposed modification. It has also been proven that the simultaneous detection of heavy metal ions is promisingly high for a nitrogen and phosphorus co-doped $Ti_3C_2T_x$ Mxene electrode as the dopants significantly boost the accessible electroactive region of the electrode in simultaneously detecting Cu^{2+} and Hg^{2+} [9].

Among numerous candidates, the electrochemically conductive and mechanically stable reduced graphene oxide (rGO) is an ideal candidate for heavy metal sensing in water. A thermally produced rGO thin film was presented by Maity et al. [10] for rapid Pb^{2+} ion detection in various water sources. Excellent Pb^{2+} detection in a 1 M HCl solution and common water samples was revealed through the employment of an electrochemically developed rGO of graphite-enforced carbon material [11]. The lowest LOD (Pb^{2+} = 0.1 g/L and Cd^{2+} = 1.0 g/L) was observed for simultaneous heavy metal ions, utilizing the micropatterned rGO, which was effectively fabricated utilizing the lithography approach [12]. Researchers discovered that the restored sp^2 carbon network in the rGO structure leads to enhanced electro-conductivity [13]. The rGO structure bound with amino groups has improved the electrode in electrically active areas. Hence, rGO can be incorporated with $Ti_3C_2T_x$ to significantly boost the electrochemical performance of the active material in the detection of heavy metal ions in water. This is because the surface area of $Ti_3C_2T_x$ MXene is significantly accessible during the process of detection, where rGO potentially serves as the spacer as well as anti-pile layer, eventually offering greater electroactive sites.

In the present work, a promising binary composite that consists of titanium-based MXene ($Ti_3C_2T_x$) and rGO was homogeneously prepared via sonication for instantaneous identification of Cu^{2+} and Cd^{2+} in water. The properties of the as-prepared $Ti_3C_2T_x$-rGO composite were characterized using XRD, FTIR, Raman, FESEM, EDX and XPS. The developed $Ti_3C_2T_x$-rGO composite was optimized by varying the ratio of $Ti_3C_2T_x$ and rGO. The optimized electroactive material was utilized for a simultaneous detection of Cd^{2+} and Cu^{2+} ions in water. $Ti_3C_2T_x$-rGO is expected to exhibit a promising limit of detection, an excellent limit of quantification along with a great electrode sensitivity towards the simultaneous heavy metal detection. $Ti_3C_2T_x$-rGO also illustrated a high peak current retention even after four weeks, signifying an outstanding electrode stability.

2. Materials and Methods

2.1. Materials

Potassium chloride (KCl, 99%) and sulphuric acid (H_2SO_4, 96%) were acquired from Fisher scientific. Meanwhile, dipotassium hydrogen phosphate (K_2HPO_4, 98%), potassium dihydrogen phosphate (KH_2PO_4, 98%) and nitric acid (HNO_3, 65%) were obtained from Merck KGaA. Sigma Aldrich supplied graphene oxide (GO, 4 mg/mL), Titanium aluminum carbide (Ti_3AlC_2, 90%), lithium fluoride (LiF, 97%), hydrochloric acid (HCl, 37%), ethanol (95%), cadmium (II) chloride ($CdCl_2$, 99.9%), and copper (II) chloride ($CuCl_2$, 99.9%). Finally, Milli-Q deionized (DI) water was obtained from Millipore (18.5 MΩ·cm, 25 °C).

2.2. Preparation of $Ti_3C_2T_x$-rGO Nanocomposite

The layered $Ti_3C_2T_x$ MXene was produced via an etching approach of the aluminium phase of MAX Ti_3AlC_2. Firstly, the etching solution was obtained by mixing LiF (1.0 g) in 9 mol/L HCl (20 mL) solution, utilizing magnetic stirring (30 min) approach. Then, 1.0 g of Ti_3AlC_2 was slowly added into the prepared mixture and allowed to stir continuously (24 h) at 35 °C to attain an impure $Ti_3C_2T_x$ MXene. The collected impure $Ti_3C_2T_x$ MXene was washed with DI water and followed by centrifuge (3500 rpm) for 10 min until it reached pH > 6.0. The pure $Ti_3C_2T_x$ MXene nanosheet dispersion was then allowed to dry utilizing a freeze dryer.

The $Ti_3C_2T_x$-rGO nanocomposite was fabricated via sonication and followed by electrochemical reduction (Figure 1a). First, the $Ti_3C_2T_x$ dispersion (3 mg/mL) was prepared by magnetically stirring $Ti_3C_2T_x$ powder (15 mg) with DI water (5 mL) for 30 min. The 3 mg/mL GO solution that sonicated for 1 h was then mixed with the 5 mL $Ti_3C_2T_x$ dispersion and proceed with ultrasonic treatment for 1 h. The prepared dispersion (5 µL) was drop-casted on a clean glassy carbon electrode (GCE) surface and allowed to dry at room temperature. GCE was polished on the polishing cloth, employing 0.5 µm of alumina slurry. The electrochemical activation of GCE was performed in 0.1 M H_2SO_4 via cyclic voltammetry (CV), applying potential from +1.5 to −0.4 V for 15 cycles. The GCE was later sonicated for 10 min each in HNO_3 and the DI water to obtain a clean electrode surface. The digital pictures in Figure 1b clearly differentiate the surface of GCE via electrode modification. The dried $Ti_3C_2T_x$-GO modified GCE was electrochemically treated in the phosphate buffer solution (PBS) (pH 7) to successfully transform GO into rGO. The chronoamperometry method (−0.8 V) was performed on the electrode for 3 min [14,15], utilized three-electrode configuration where the $Ti_3C_2T_x$-GO coated GCE, platinum (Pt) wire and silver/silver chloride (Ag/AgCl) acted as the working electrode, counter electrode and reference electrode, respectively. The produced $Ti_3C_2T_x$-rGO nanocomposite was labelled as the working electrode in this application.

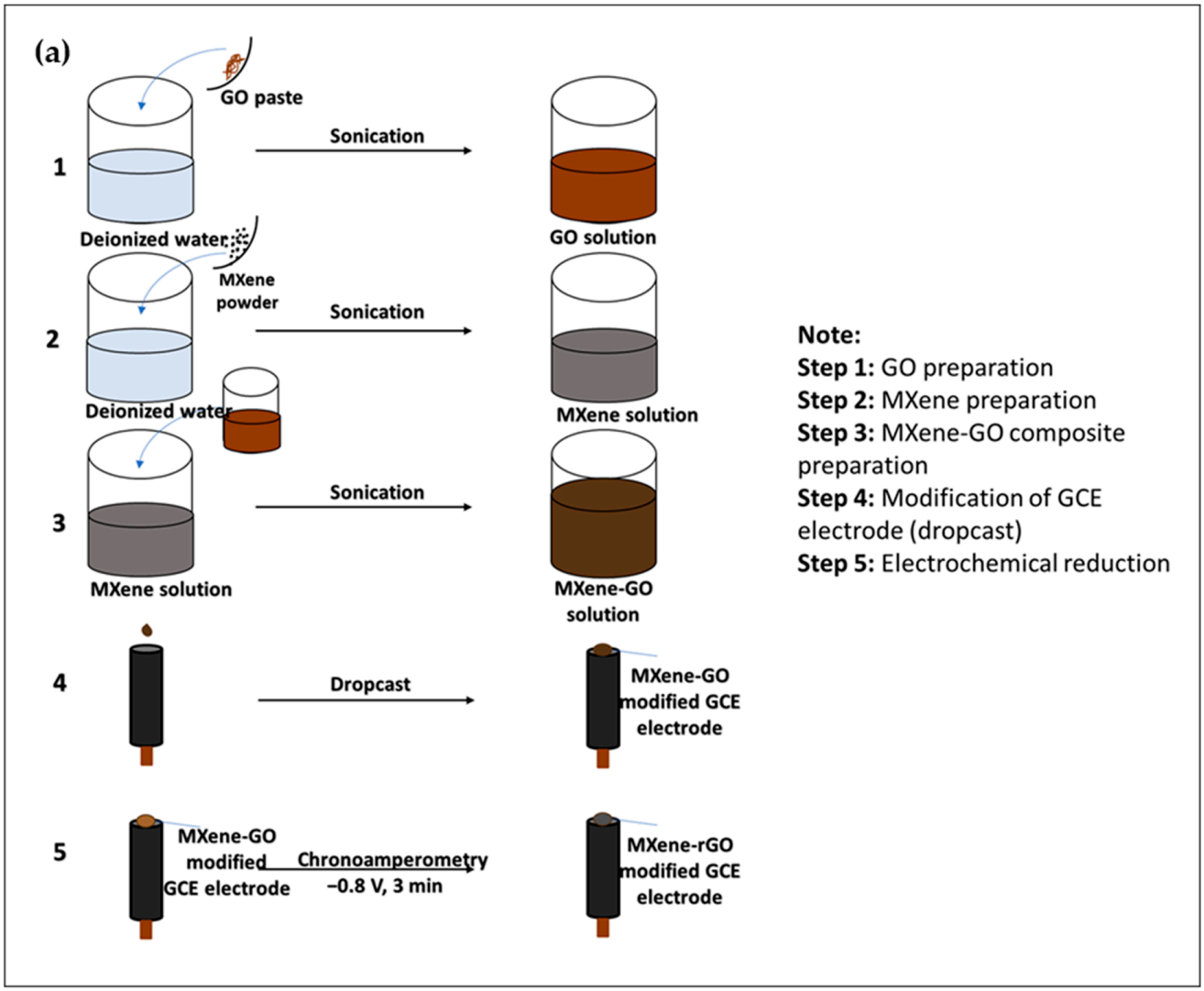

Figure 1. (**a**) Schematic diagram illustrates the synthesis of $Ti_3C_2T_x$-rGO nanocomposite. (**b**) Digital photographs demonstrate the surface of GCE before (**left**) and after (**right**) modification process. (**c**) The three-electrode system setup of the electrodes for electrochemical analysis (pH study).

2.3. $Ti_3C_2T_x$-rGO Nanocomposite Characterization

X-ray diffraction analysis was conducted to examine the phase composition of the synthesized samples using Bruker X-ray diffractometer D8 advance. The vibration modes and functional groups signals of the materials were retrieved from Raman spectroscopy

(Thermo Scientfific Raman spectrometer, 488 nm) and Fourier Transform Infrared Spectrometer (FTIR, Perkin-Elmer Spectrum100), respectively. The field emission scanning microscopy (FESEM, ZEISS MERLIN) and X-ray photoelectron spectroscopy (XPS, XSAMHS Kratos Analytical) were performed to determine the morphological and the chemical compositions of the composite surfaces, respectively.

2.4. Electrochemical Detection of Heavy Metals

The prepared binary $Ti_3C_2T_x$-rGO composite was investigated for simultaneous heavy metal detection, namely, Cd^{2+}, and Cu^{2+} ions in water sample. Various analysis was conducted to investigate the performance of $Ti_3C_2T_x$-rGO on the detection of analytes. All electrochemical analyses were performed via potentiostat (Autolab PGSTAT204), utilizing electroactive material coated GCE (working electrode), Pt wire (counter electrode) and Ag/AgCl (reference electrode); in a three-electrode configuration). Differential pulse voltammetry (DPV) assessments were conducted for the proposed $Ti_3C_2T_x$-rGO electrode at a potential ranging from -0.95 to -0.05 V for pH study to determine the optimum pH of PBS for the simultaneous copper (Cu^{2+}) and cadmium (Cd^{2+}) ions detection. The potential range was then widened from -0.95 to +0.1 V for the concentration study, real sample study, interference study, reproducibility test, repeatability test and stability test in this sensor application. The simultaneous heavy metal ions detection process began with a pre-electroreduction step, where a potential of –0.95 V (vs Ag/AgCl) was applied using DPV. In this work, the detection of Cu^{2+} and Cd^{2+} ions using a MXene/rGO composite electrode via DPV is typically carried out under careful optimized experimental conditions to achieve high sensitivity and selectivity towards the heavy metal ions detection. The actual experimental conditions of this work were properly developed following strict and standard procedures. The effect of supporting electrolyte pH on the voltametric response of the mixture of Cd^{2+}, and Cu^{2+} on the prepared electrode was evaluated in the PBS (pH 4–6.5 (Figure 1c)). The DPV signal of the proposed electrode was recorded for various pH of PBS containing heavy metal ions.

The concentration study was carried out by increasing the concentration of both analyte (Cd^{2+} and Cu^{2+}) in the optimized condition. A calibration curve was obtained from the relationship between the same analyte concentration against the produced oxidation peak current and the error bars (relative standard deviation), where it was generated for each concentration of analyte. This analysis was conducted via DPV method at 50 mV pulse amplitude, 50 ms pulse width and 20 mV/s scan rate. The reproducibility of electrochemical sensor was examined by measuring the analytes using five different electrodes and the relative standard deviation (RSD) was calculated. Repeatability of the sensor was evaluated by recording ten successive measurements using the same electrode. Stability of the electrochemical sensor was studied by preparing different electrodes and storing it at room temperature for a period of time. The current response of the stored electrodes was recorded after 1 week, 2 weeks, 3 weeks and 4 weeks via DPV analysis. The percentage for signal change was calculated and compared in continuous 4 weeks.

3. Result and Discussion

3.1. Characterization

Figure 2 demonstrates XRD diffraction peaks of various samples. This analysis was conducted to determine the sample phase compositions. The Ti_3AlC_2 illustrates XRD diffraction peaks at 9.5° (002), 18.9° (004), 34.0° (101), 38.9° (104), 41.8° (105), 48.4° (107), 56.5° (109) and 60.7° (110), which matches well with the JCPDS pattern 052-0875 of Ti_3AlC_2 (hexagonal lattice) [16]. The $Ti_3C_2T_x$ MXene produced through etching process demonstrates (002), (004), (101), (104), (105), (107), (109) and (110) planes at 8.3°, 19.1°, 34.0°, 38.7°,

41.8°, 48.4°, 56.4° and 60.5°, respectively. The diminished (104) plane of $T_3C_2T_x$ and the (002) plane of $Ti_3C_2T_x$ MXene is noticeably lower in intensity and broader in peak at 8.3°, signifying the successful Al-etching of Ti_3AlC_2 [17,18]. GO illustrates a diffraction peak at 10.2°, indicating the lattice plane (001) [19–21]. An effective electrochemical reduction procedure results in a wide rGO diffraction peak at 2θ = 25.3° (002), indicating the presence of graphite-like sheets [14,22,23]. The $Ti_3C_2T_x$-rGO illustrates all XRD signals of $Ti_3C_2T_x$ and rGO, validating a successful formation of the sample.

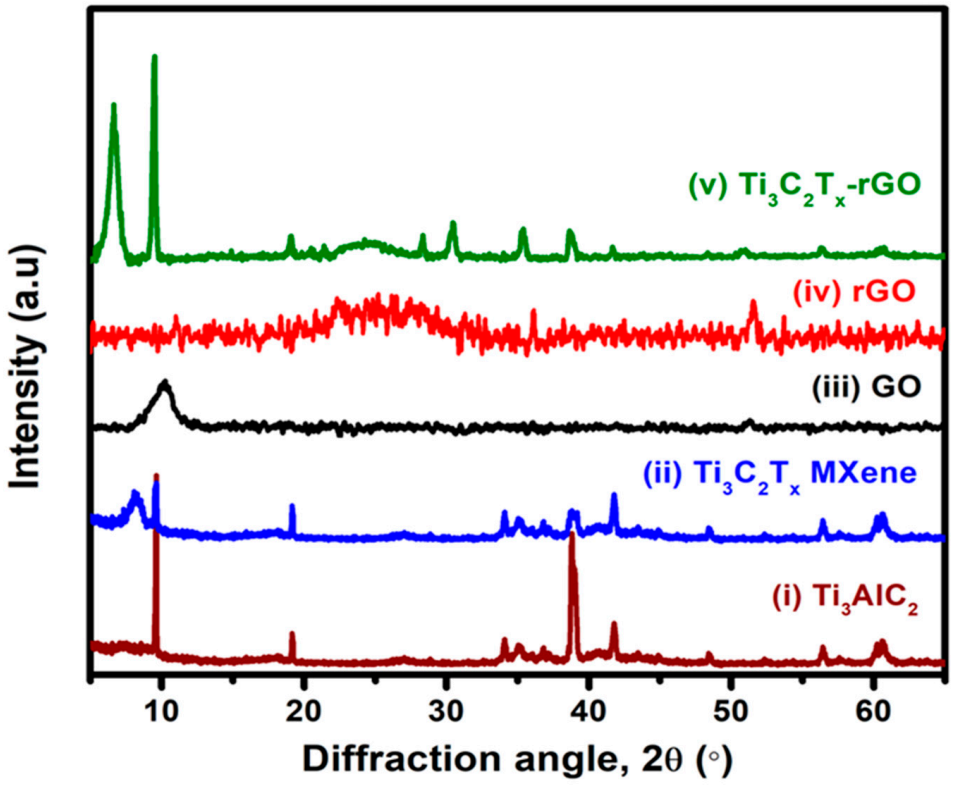

Figure 2. XRD spectra of Ti_3AlC_2, $Ti_3C_2T_x$ MXene, GO, rGO and $Ti_3C_2T_x$-rGO.

The vibration modes within the as-prepared materials were investigated via Raman spectroscopy (Figure 3a. A strong D band (sp^3-hybridized carbon) and G band (sp^2-hybridized carbon) are observed for GO (D band = 1355 cm^{-1} and G band = 1594 cm^{-1}) and rGO (D band = 1354 cm^{-1} and G band = 1594 cm^{-1}) samples. The band intensity ratio of D over G (I_D/I_G) can be adopted to estimate the degree of disorder in the graphite structure. The ratio value of I_D/I_G larger than 1 signifies that the sample comprises more sp^3-hybridized carbon atoms than sp^2-hybridized carbons [24–26]. The measured I_D/I_G ratio of GO is 0.94, whereas the I_D/I_G ratio of rGO (1.24) and $Ti_3C_2T_x$-rGO (1.32) confirm that the proposed electrochemical reduction process diminished oxygenated functional groups that was originally appear on the GO layer [27]. $Ti_3C_2T_x$ MXene depicts Raman peaks at 147.8, 279.4, 391.5, 591.0 cm^{-1} correspond to the low levels of anatase TiO_2 on the outermost surface of $Ti_3C_2T_x$ MXene [28]. The Raman signal at 721.8 cm^{-1} shows the A_{1g} symmetrical out-of-plane vibration of Ti and C atoms [29]. The D band and G band of $Ti_3C_2T_x$ MXene are observed at 1325.2 and 1559.8 cm^{-1}, where the D band represents disorder induction within the structure. The synthesized $Ti_3C_2T_x$-rGO illustrates all the characteristic peaks of $Ti_3C_2T_x$ and rGO.

Figure 3b represents the FTIR spectra of GO, rGO, $Ti_3C_2T_x$ MXene, and $Ti_3C_2T_x$-rGO electrodes. GO demonstrates C-O-C, C=C, C=O and O-H functional groups at 1057, 1387, 1621 and 3301 cm^{-1}, respectively. After reduction reaction, rGO illustrates peaks

at 1047 cm^{-1} (C-OH), 1363 cm^{-1} (C=C), 1597 cm^{-1} (C=O) and 3307 cm^{-1} (O-H). The intensity of O-H (3307 cm^{-1}) carboxyl stretching mode of rGO is noticeably smaller than the GO (3301 cm^{-1}), validating successful electrochemical reduction process. The Ti-O (667 cm^{-1})and C=O (1640 cm^{-1}) vibration modes are clearly seen from $Ti_3C_2T_x$ MXene. The existence of hydroxyl groups is verified by the absorption signals at 3301 and 1640 cm^{-1}, which are ascribed to the absorbed external water and highly hydrogen-bonded OH or exceptionally strong coordinated H_2O in the $Ti_3C_2T_x$ MXene. The detected FTIR signal of $Ti_3C_2T_x$-rGO further affirms the formation of the composite.

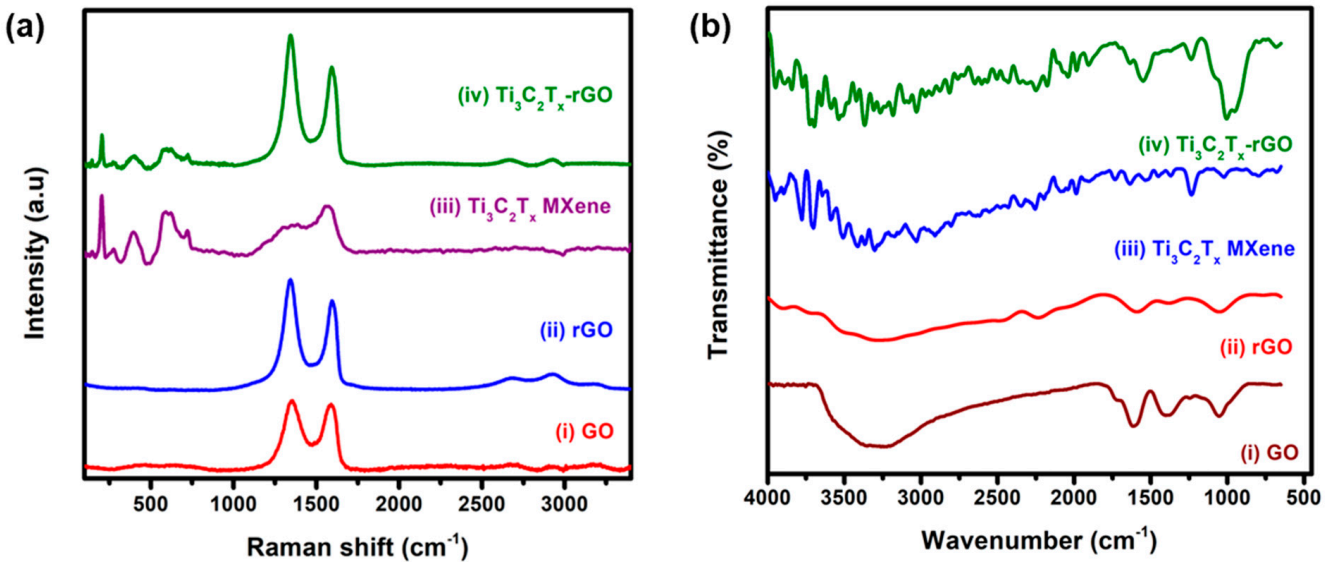

Figure 3. (**a**) Raman and (**b**) FTIR spectra of GO, rGO, $Ti_3C_2T_x$ MXene, and $Ti_3C_2T_x$-rGO.

Identification of the surface morphology of the as-prepared samples was performed using FESEM analysis and presented in Figure 4. Both GO (Figure 4a) and rGO (Figure 4b illustrate wrinkle-like morphology. The inset of Figure 4b denotes that the rGO has a more pronounced wrinkle-like morphology compared to the GO, which is the result of the successful electrochemical reduction process [19,30]. This statement is in good agreement with the XRD, FTIR and Raman results. $Ti_3C_2T_x$ (Figure 4c depicts a multi layered MXene flakes morphology after a successful chemical etching. Whereas, the $Ti_3C_2T_x$-rGO composite (Figure 4d) which is prepared through simple sonication method, shows that the rGO sheet uniformly covers the multi layered MXene flakes.

$Ti_3C_2T_x$-rGO composite was further evaluated through an elemental mapping as depicted in Figure 5a. Titanium (Ti), Carbon (C), Oxygen (O) and Aluminum (Al) are noticed from the analysis, and it can be clearly spotted that all the elements are distributed evenly on the composite, confirming homogeneous formation of the composite. The Al signal still can be observed in the $Ti_3C_2T_x$-rGO composite even after the Al-etching indicates that there is incomplete etching process at the inner layers of Ti_3AlC_2 [31]. From the EDX analysis (Figure 5b) of $Ti_3C_2T_x$-rGO composite, Ti, C, O, and Al are successfully recorded with the respective weight percentage of 88.1, 10.3, 1.5 and 0.1%. EDX result revealed that only minimal amount of Al (0.1%) present within the composite, confirming a successful etching of Al and there are still few unetched Al within the inner structure of $Ti_3C_2T_x$ MXene.

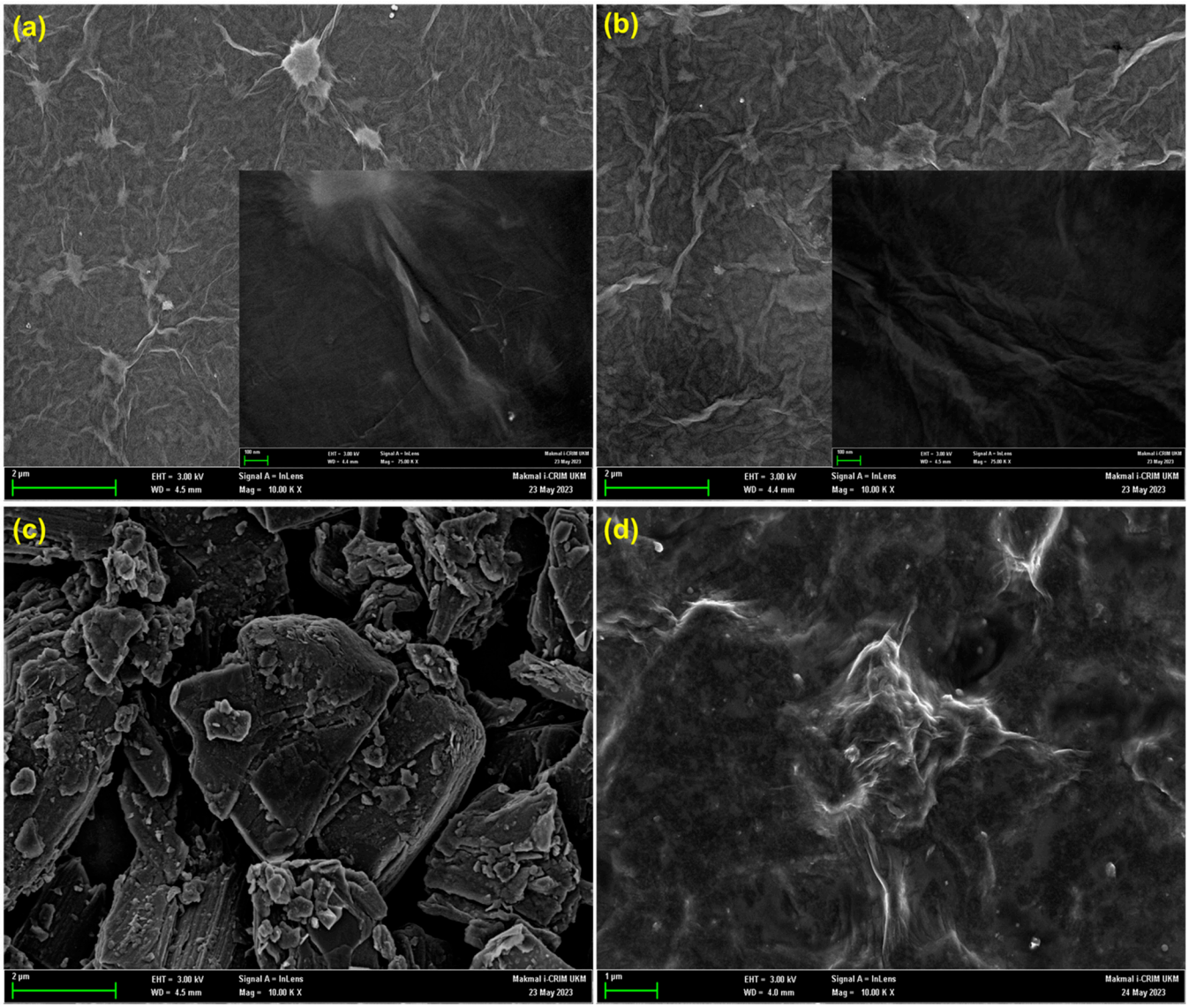

Figure 4. FESEM images of (**a**) GO (inset: GO at higher magnification), (**b**) rGO (inset: rGO at higher magnification, (**c**) $Ti_3C_2T_x$, and (**d**) $Ti_3C_2T_x$-rGO.

The chemical composition of the as-prepared $Ti_3C_2T_x$-rGO composite was investigated via XPS analysis (Figure 6). Ti2p, C1s and O1s signals are obtained at the binding energy of 458, 285 and 529 eV, respectively (Figure 6a). Ti2p signal originates from $Ti_3C_2T_x$ MXene, while C1s and O1s are produced by both $Ti_3C_2T_x$ and rGO. The $Ti2p_{1/2}$ and $Ti2p_{3/2}$ characteristics are observed from Figure 6b. The deconvolution of Ti2p spectrum depicts seven different peaks, which appears at the binding energy of 454.7 (Ti-C $2p_{3/2}$), 455.2 (Ti(II)), 456.5 (Ti-O $2p_{3/2}$), 459.2 (TiO_2), 461.1 (Ti-C $2p_{1/2}$), 461.9 (Ti(III)), 463.3 eV (Ti-O $2p_{1/2}$) [32–35]. The C1s spectrum presented in Figure 6c illustrates four deconvoluted XPS peaks, which indicates the C=C/C–C, C–O (epoxy and hydroxy), C=O and O–C=O interactions happen at specific binding energies of 281.4, 282.1, 284.6 and 286.2 eV, respectively. From the result, it can be clearly seen that the intensity of C-C/C=C signal is relatively higher than the C-O (hydroxy and epoxy), revealing a successful reduction of GO. It also proves that the rGO within the composite still consist of several oxygen-containing functional groups [36]. The O1s spectrum (Figure 6d) is deconvoluted into four peaks that are clearly noticed at the binding energy of 529.7 eV (O-Ti), 530.6 eV (C-Ti-O_x), 531.4 eV (C-Ti-OH_x) and 532.7 eV (H_2O-Ti) [32]. The XPS result affirms that the $Ti_3C_2T_x$ MXene is successfully obtained via a chemical synthesis route. The electrochemical reduction

effectively reduced GO to rGO without disturbing the structure of $Ti_3C_2T_x$ MXene. The XPS signal is also in full alignment with the XRD, FTIR, Raman, FESEM, EDX and elemental mapping results presented earlier.

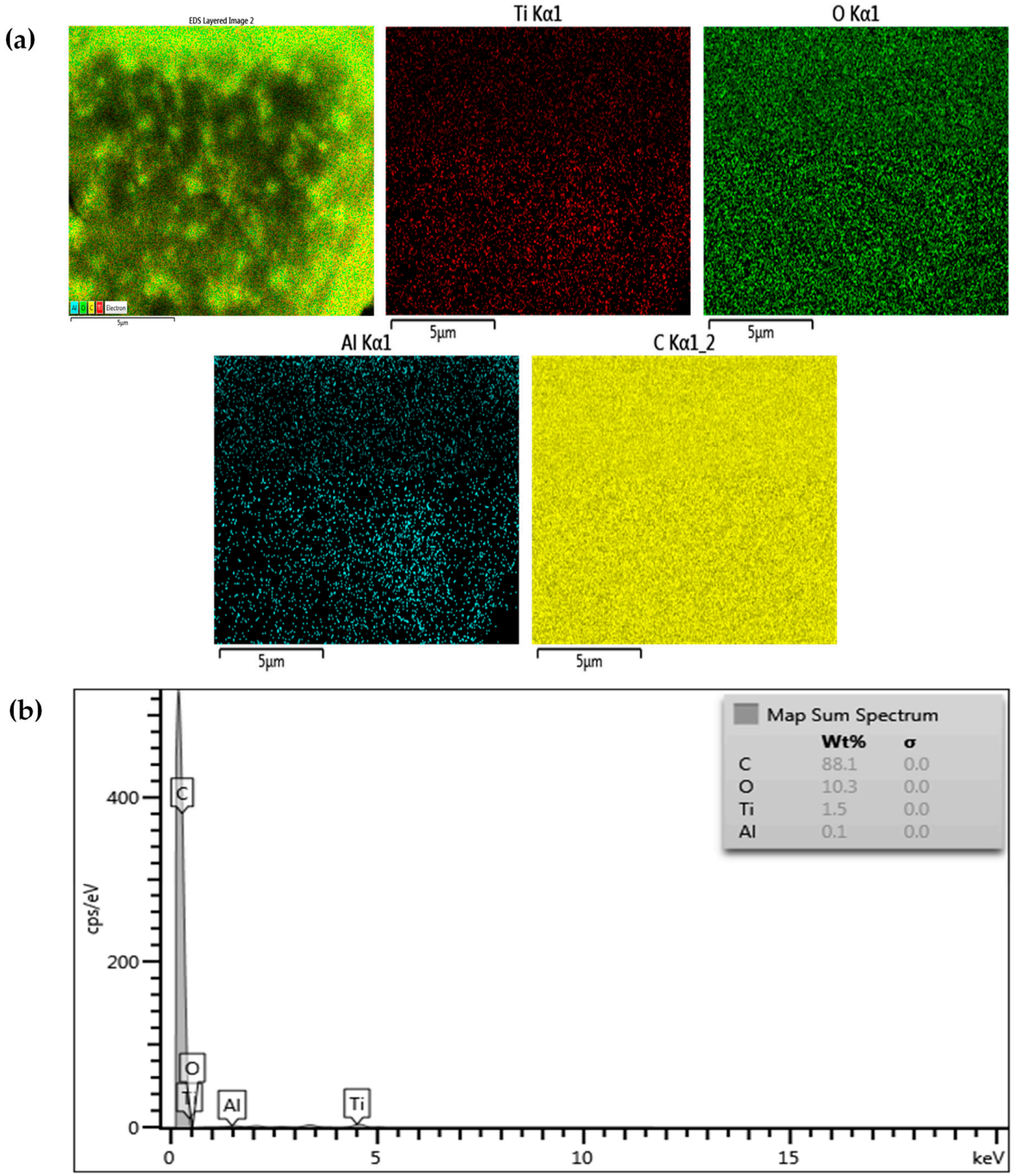

Figure 5. (**a**) Elemental mapping (elements: Ti, C, O, Al) of $Ti_3C_2T_x$-rGO composite, and (**b**) EDX of $Ti_3C_2T_x$-rGO composite.

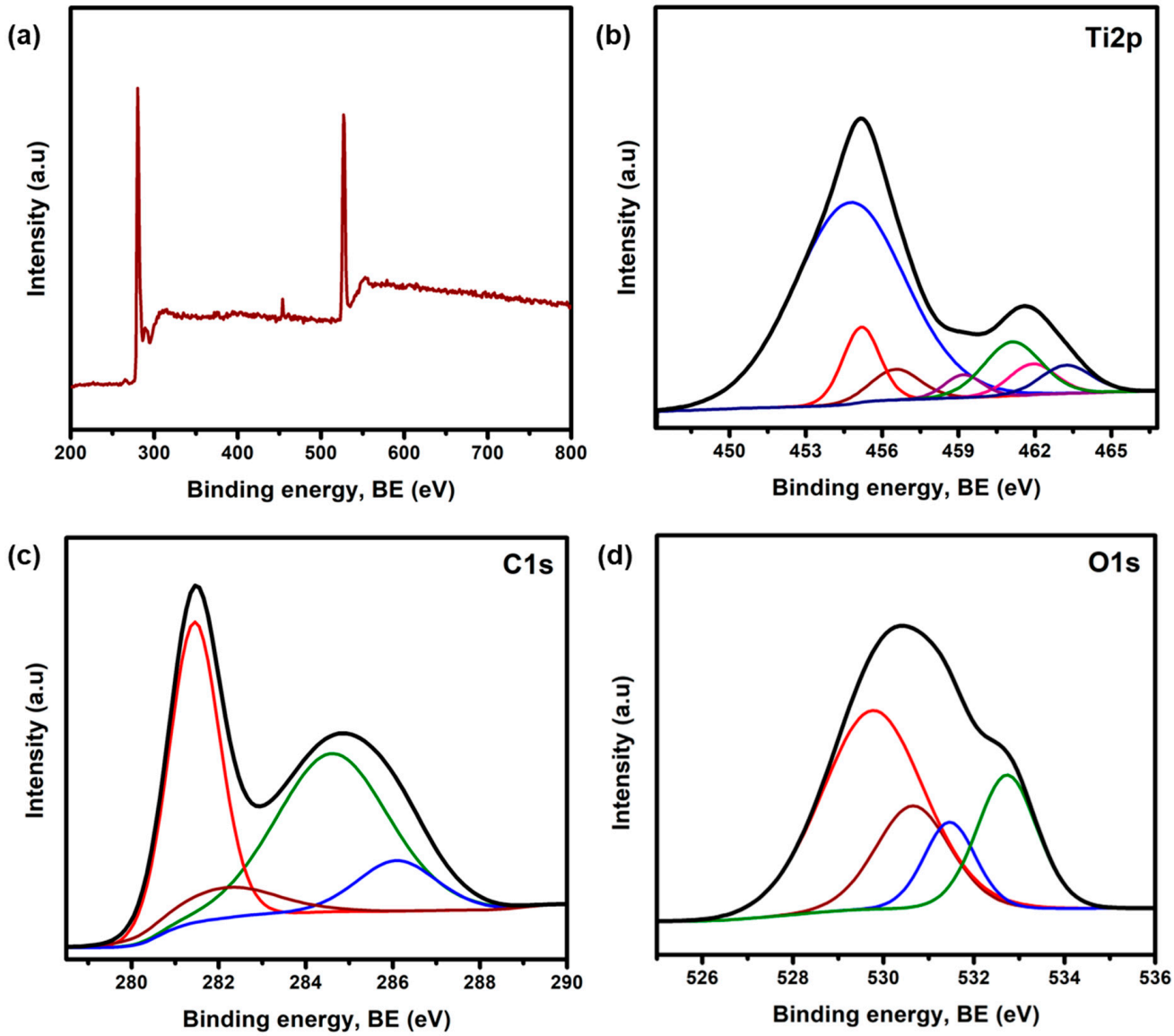

Figure 6. (**a**) Wide scan XPS spectra and the high resolution (**b**) Ti2p, (**c**) C1s, and (**d**) O1s, of $Ti_3C_2T_x$-rGO composite.

3.2. Electrochemical Detection

Figure 7a depicts the DPV curve of bare GCE, rGO, $Ti_3C_2T_x$ MXene, and $Ti_3C_2T_x$-rGO electrodes for the detection of 1 mM Cd^{2+} and Cu^{2+} in PBS (pH = 5.0). An obvious and low intensity Cd^{2+} signal and a broad and weak Cu^{2+} peak is obtained for bare GCE at the respective values of −0.74 and −0.16 V. Comparatively, the Cd^{2+} ion peak current is noticeably higher than the Cu^{2+} ion, indicating the difference in sensitivity of electrode for both the heavy metal ions. The introduction of $Ti_3C_2T_x$ or rGO on a bare GCE illustrates an evident spike in peak currents and increase in the electrochemical signal through instantaneous ions detection, caused by the higher electrocatalytic activity and enhanced electrochemical surface area of the electrode. On the other hand, the pristine GCE, $Ti_3C_2T_x$ MXene demonstrates prominent absorption peaks at the respective −0.75 and −0.17 V that indicate the peak of Cd^{2+} and Cu^{2+}. Meanwhile, the Cu^{2+} signal is found weak for rGO. Therefore, the integration of $Ti_3C_2T_x$ and rGO to form $Ti_3C_2T_x$-rGO composite has resulted in greater peak currents as the rGO increased the interlayer spacing of $Ti_3C_2T_x$, creating vast surface area for a better interaction of Cd^{2+} and Cu^{2+} [37]. Result implies that the $Ti_3C_2T_x$-rGO displays high intensity peak current than the $Ti_3C_2T_x$, rGO and bare

GCE. Interestingly, $Ti_3C_2T_x$-rGO shows completely separated and intense peak currents that improve the detection of Cu^{2+} and Cd^{2+} ions electrochemically. The synergistic effect within the $Ti_3C_2T_x$-rGO electrode leads to outstanding oxidation signals towards Cd^{2+} and Cu^{2+} ions.

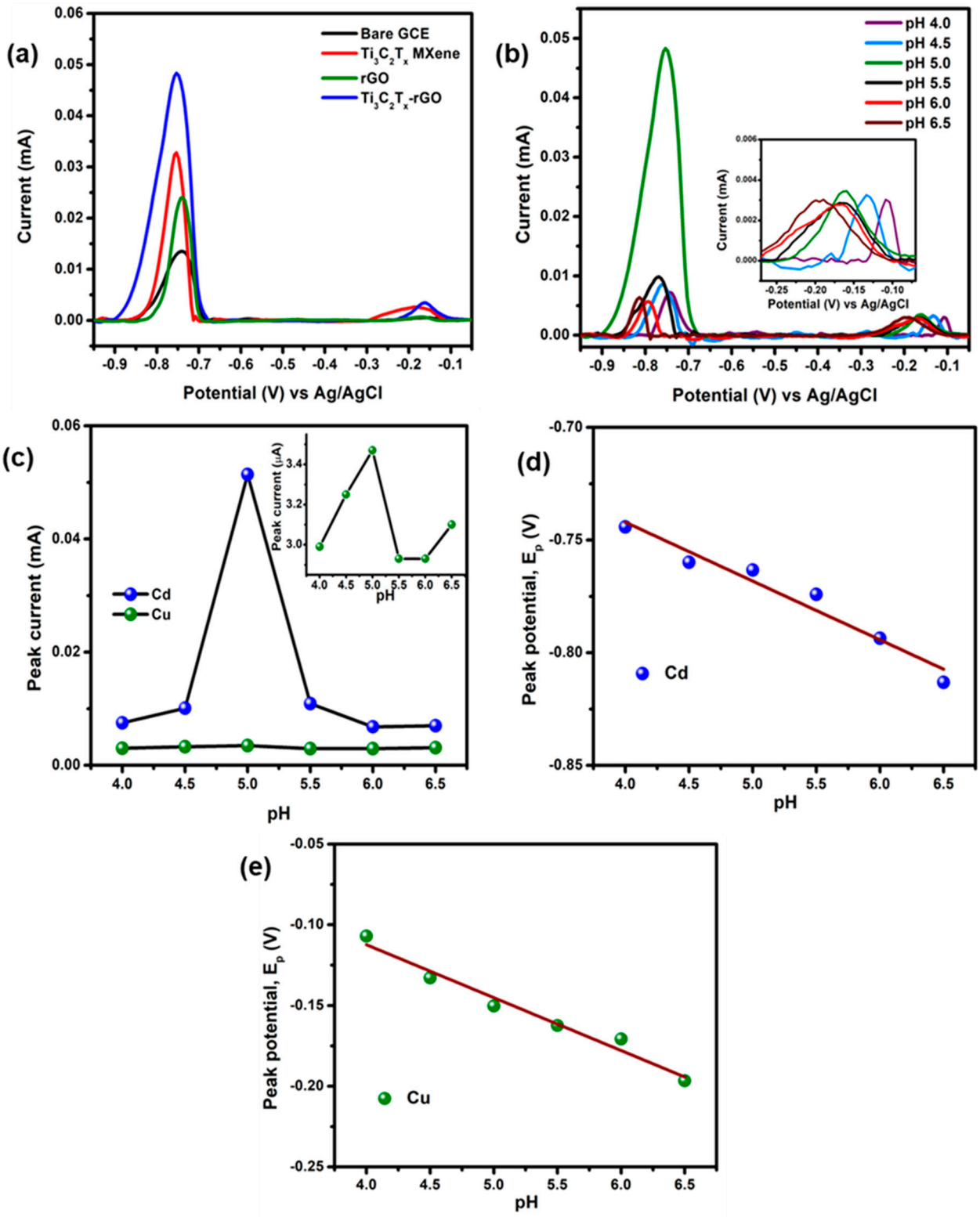

Figure 7. Differential pulse voltammogram of (**a**) various electroactive materials at pH 5 and (**b**) $Ti_3C_2T_x$-rGO composite in PBS (1 mM Cd^{2+} and 1 mM Cu^{2+}) altering the pH from 4 to 6.5. (**c**) PBS pH on the peak current of Cd^{2+} and Cu^{2+} effect (inset detailed Cu peak current response against the pH) and impact of PBS pH on the peak potential of (**d**) Cd^{2+} and (**e**) Cu^{2+}.

Figure 7b demonstrates the DPV of $Ti_3C_2T_x$-rGO composite immersed in the PBS consisting of 1mM Cd^{2+}-Cu^{2+} within the pH range of 4.0 to 6.5. The redox reactions under the proton influence causes slight shifting in peak potentials of Cd^{2+}-Cu^{2+} at the negative potential as the pH of the PBS rises [38,39]. This is because the presence of protons in the PBS reduces as the pH of the solvent rises. The formation of Cd^{2+} and Cu^{2+} ions from its metallic forms (Cu^0 and Cd^0) is rapid in the high pH PBS. The transformed heavy metal ions develop an electrostatic repulsion within Cd^{2+}, Cu^{2+} as well as $Ti_3C_2T_x$-rGO composite, causing difficulty for electrochemical reaction to occur at high pH with low peak currents. Figure 7c illustrates the peak current versus pH of Cd^{2+} and Cu^{2+}. The peak currents for Cd^{2+} and Cu^{2+} intensified when the pH elevated from 4 to 5, potentially due to the competition between the targeted heavy metal ions and protons for the binding sites on the electrode surface [40]. This phenomenon is due to the increase of pH of the PBS, which has resulted in the amount of proton present in the analyte solution to decrease. The Cd^{2+} and Cu^{2+} signals from pH 5.5 to 6.5 are observed with low peak currents, which is due to the hydrolysis of heavy metal ions [41,42]. The ideal pH used for this task is pH 5 as it illustrates highest peak current of 51.4 and 3.47 µA for Cd^{2+} and Cu^{2+}, respectively. The relationship of the peak potential (E_p) of Cd^{2+} and Cu^{2+} versus pH is demonstrated in Figure 7d–e. The E_p of both Cd^{2+} and Cu^{2+} are noticeably proportional to the PBS pH in accordance with the regression equation of E_p (V) = −0.046 pH−0.637 (R^2 = 0.989) for Cd^{2+} and E_p (V) = −0.042 pH + 0.018 (R^2 = 0.967) for Cu^{2+}, respectively.

The simultaneous detection of Cd^{2+} and Cu^{2+} was performed via DPV analysis (Figure 8a) utilizing $Ti_3C_2T_x$-rGO. Figure 8a depicts the Cd^{2+} and Cu^{2+} ions detection in PBS (pH 5), varying the concentration of Cd^{2+} (7.5–150 nM) and Cu^{2+} (1–150 nM). Figure 8b,d displays differential pulse voltammograms that focus on $Ti_3C_2T_x$-rGO composite in various Cd^{2+} and Cu^{2+} concentrations ranging from 7.5 to 150 nM and 1 to 150 nM, respectively. Result implies that the peak current of Cd^{2+} and Cu^{2+} increases with increasing concentration [43]. The plot of peak current against concentration of Cd^{2+} and Cu^{2+} is exhibited in Figure 8c,e, respectively. The Cd^{2+} peak currents rise gradually with the concentration of Cd^{2+} and the correlation between peak current with Cd^{2+} concentration shall be potentially represented in the form of I_{pa} (µM) = 0.345 Cd^{2+} (µM) + 0.010 with R^2 = 0.999. The sensitivity of $Ti_3C_2T_x$-rGO against Cd^{2+} is 0.345 µMµA^{-1}, which is attained from the slope of the equation. Similarly, the peak currents of Cu^{2+} constantly increase as the concentration of Cu^{2+} rises. Cu^{2+} also shows a straight-line curve of peak current and Cu^{2+} concentration, that is presented as I_{pa} (µM) = 0.575 Cu^{2+} (µM) + 0.158 where R^2 = 0.993. The achieved sensitivity of $Ti_3C_2T_x$-rGO towards the detection of Cu^{2+} is 0.575 µMµA^{-1}. It can be concluded that the modified $Ti_3C_2T_x$-rGO electrode is capable to demonstrate a complete-separation of oxidation peak and the electrochemical detection of Cd^{2+} and Cu^{2+} that does not interfere with each other. Limit of detection (*LOD*) and limit of quantification (*LOQ*) are measured via Equations (1) and (2), where σ and s are standard deviation and slope of the calibration curve, respectively. The *LOD* of $Ti_3C_2T_x$-rGO modified electrode for Cd^{2+} and Cu^{2+} are 0.31 and 0.18 nM, respectively. Whereas the *LOQ* discovered for Cd^{2+} and Cu^{2+} are 1.02 and 0.62 nM, respectively. The performance of the suggested $Ti_3C_2T_x$-rGO composite and the other modified electrodes in detecting Cd^{2+} and Cu^{2+} is tabulated in Table 1. The $Ti_3C_2T_x$-rGO composite result is found comparable with the reported literature. The proposed electroactive material in this work also demonstrates an outstanding *LOD* for simultaneous heavy metals detection, which is significantly lower than the other reported MXene based composites.

$$LOD = \frac{3\sigma}{s} \quad (1)$$

$$LOQ = \frac{10\sigma}{s} \quad (2)$$

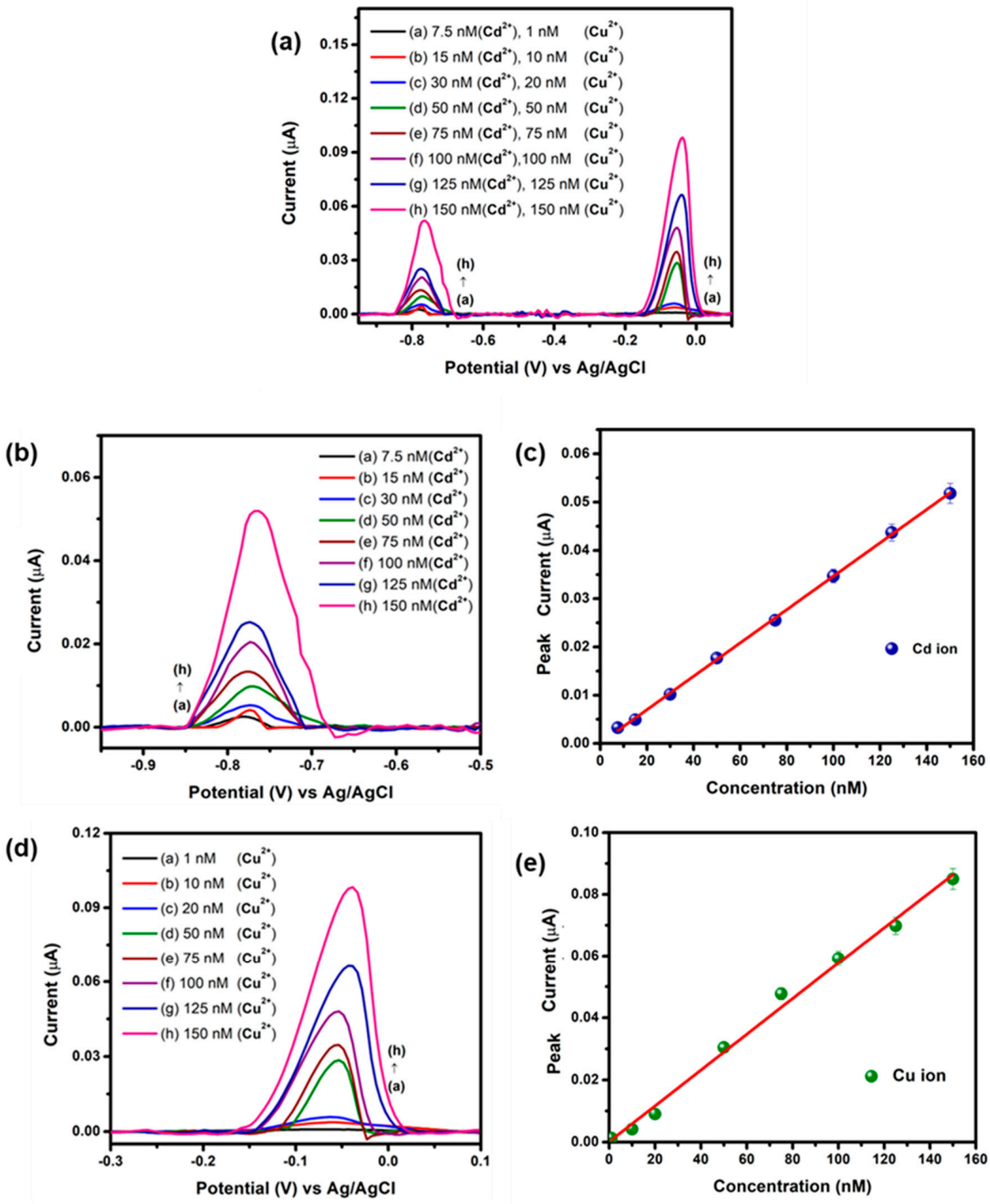

Figure 8. (**a**) DPV response of $Ti_3C_2T_x$-rGO electrode for the detection of Cd^{2+} and Cu^{2+} in the PBS (pH 5). DPV plot of $Ti_3C_2T_x$-rGO electrode at different concentrations for (**b**) Cd^{2+} (7.5–150 nM) and (**d**) Cu^{2+} (1–150 nM) detection with the calibration plot for both (**c**) Cd^{2+} and (**e**) Cu^{2+} with error bar: standard deviation for $n = 3$.

The reproducibility of $Ti_3C_2T_x$-rGO was determined by testing 0.5 mM Cd^{2+} and Cu^{2+} using five distinct electrodes and the calculated relative standard deviation (RSD)

of 2.42% and 2.36% are attained for Cd^{2+} and Cu^{2+}, respectively. The repeatability of $Ti_3C_2T_x$-rGO, is evaluated at 10 DPV signal using a similar electrode and this test is performed in the 0.5 mM solution of Cd^{2+} and Cu^{2+}. The calculated RSD are 1.93% and 3.58% for Cd^{2+} and Cu^{2+}, respectively, signifying outstanding repeatability of the proposed material. The $Ti_3C_2T_x$-rGO sensor constancy was determined upon testing 0.1 mM Cd^{2+} and 0.1 mM Cu^{2+} in the pH 5 PBS. Although the approximate concentration of dissolved oxygen in water at room temperature and 1 atm pressure is around 0.25 mM, even nanomolar concentrations of metal ions can significantly suppress the oxygen signal observed in DPV. This seemingly disproportionate effect arises from several electrochemical and chemical interactions. Certain metal ions, such as Cu^{2+}, Fe^{2+}, or Mn^{2+}, can catalyze the oxygen reduction reaction (ORR), to alter the kinetics and mechanisms of oxygen's electrochemical behaviors. These ions can form transient complexes with oxygen or its reduction intermediates, thereby modifying the redox potential and diminishing the distinct oxygen peak in DPV. Additionally, metal ions can adsorb onto the electrode surface and alter its electrochemical properties, including electron transfer rates and surface reactivity. This surface modification can hinder the reduction of oxygen or shift its peak, leading to apparent suppression. Despite their low concentration, these ions can exert a catalytic or a surface-blocking effect that disrupts the sensitivity and resolution of DPV, which is a highly sensitive technique designed to detect subtle changes in current. Thus, the suppression of oxygen signals by trace metal ions highlights the importance of understanding both direct and indirect interactions in electrochemical analyses.

Table 1. Performance of various MXene-based electrodes for heavy metal detection.

No.	Material	Heavy Metal Detected	*LOD* (nM)	Linear Range of Detection (μM)	Reference
1	alk-Ti_3C_2	Cu^{2+} Cd^{2+}	39.00 82.00	0.1–1.4 μM 0.1–1.4 μM	[44]
2	H–C_3N_4/$Ti_3C_2T_x$	Cd^{2+} Pb^{2+}	1.00 0.60	0.5–1.5 μM 0.5–1.5 μM	[45]
3	Ti_3C_2@N-C	Cd^{2+} Pb^{2+}	2.25 1.10	0.1–4 μM 0.05–2 μM	[46]
4	BiNPs/$Ti_3C_2T_x$	Cd^{2+} Pb^{2+}	12.4 10.8	0.08–0.8 μM 0.06–0.6 μM	[47]
5	**$Ti_3C_2T_x$-rGO**	**Cd^{2+}** **Cu^{2+}**	**0.31** **0.18**	**7.5–150 nM** **1–150 nM**	**This work**

alk-Ti_3C_2: alkaline intercalation of Ti_3C_2, H–C_3N_4/$Ti_3C_2T_x$: protonated carbon nitride/$Ti_3C_2T_x$, Ti_3C_2@N-C: nitrogen-doped carbon-coated Ti_3C_2-MXene, BiNPs/$Ti_3C_2T_x$: bismuth-nanoparticles/$Ti_3C_2T_x$.

Next, the prepared sensor was stored for 30 days at atmospheric temperature and the detailed peak current retention (%) of $Ti_3C_2T_x$-rGO is tabulated in Table 2. Result shows that $Ti_3C_2T_x$-rGO electrode retained 97.86% (Cd^{2+}) and 98.01% (Cu^{2+}) of its initial peak current responses, implying excellent stability of $Ti_3C_2T_x$-rGO towards simultaneous detection Cd^{2+} and Cu^{2+}.

Table 2. Stability study of $Ti_3C_2T_x$-rGO electrode for the detection of Cd^{2+} and Cu^{2+}.

Stability Period	Peak Current Retention (%)	
	Cd^{2+}	Cu^{2+}
1 Week	98.19%	99.81%
2 Week	98.61%	99.48%
3 Week	99.89%	98.49%
4 Week	97.86%	98.01%

The impact of various interference ions in the PBS containing 1 mM Cd^{2+} and Cu^{2+} were investigated using $Ti_3C_2T_x$-rGO. The 100-fold and 1000-fold concentration of the interference ions (Na^+, K^+, Ca^{2+}, Mg^{2+}, Cl^-, $SO_4{}^{2-}$) were tested and the result shows that the injected ions do not interfere in a simultaneous detection of Cd^{2+} and Cu^{2+} ions in PBS (pH = 5) where the signal change is less than 5% [39]. An excellent interference resistance disclosed that the $Ti_3C_2T_x$-rGO is reliable even under ambient conditions. The practical effectiveness of $Ti_3C_2T_x$-rGO for simultaneous Cd^{2+} and Cu^{2+} detection has been explored by employing lake water and tap water. A predetermined quantity of Cd^{2+} and Cu^{2+} was injected into the solution for the purpose of the recovery experiment, which was carried out using DPV analysis. The quantity of Cd^{2+} and Cu^{2+} found in lake and supplied drinking water was identified using the traditional addition technique, and the recovery of Cd^{2+} and Cu^{2+} in percentage ranged between 96% and 99.5% (Tables 3 and 4). The results show that the $Ti_3C_2T_x$-rGO composite can detect Cd^{2+} and Cu^{2+} simultaneously using actual water samples.

Table 3. Recover data on concurrent detection of Cd^{2+} and Cu^{2+} in lake water (n = 3).

Sample	Added (nM)		Obtained (nM)		Recovery (%)	
	Cd^{2+}	Cu^{2+}	Cd^{2+}	Cu^{2+}	Cd^{2+}	Cu^{2+}
1	60	60	58.4	58.9	97.3%	98.2%
2	80	80	78.1	79.3	97.6%	99.1%
3	100	100	98.9	99.5	98.9%	99.5%

Table 4. Recover data on concurrent detection of Cd^{2+} and Cu^{2+} in tap water (n = 3).

Sample	Added (nM)		Obtained (nM)		Recovery (%)	
	Cd^{2+}	Cu^{2+}	Cd^{2+}	Cu^{2+}	Cd^{2+}	Cu^{2+}
1	60	60	58.7	57.6	97.8%	96.0%
2	80	80	78.2	78.3	97.8%	97.9%
3	100	100	99	98.8	99.0%	98.8%

4. Conclusions

A promising $Ti_3C_2T_x$-rGO sensor for Cd^{2+} and Cu^{2+} detection was successfully developed employing chemically synthesized $Ti_3C_2T_x$ and electrochemically produced rGO by demonstrating obvious and intense Cd^{2+} and Cu^{2+} oxidation peaks via DPV analysis. $Ti_3C_2T_x$-rGO composite revealed significant electro-chemical-catalytic activity with respect to the Cd^{2+} and Cu^{2+} oxidation. It is also found that the $Ti_3C_2T_x$-rGO composite with improved electron transfer characteristics in comparison to the bare GCE, $Ti_3C_2T_x$ and rGO. The results demonstrate a significantly low *LOD* and *LOQ* for concurrent detection of Cd^{2+} (*LOD* = 0.31 nM, *LOQ* = 1.02 nM) and Cu^{2+} (*LOD* = 0.18 nM, *LOQ* = 0.62 nM) ions in water. The promising $Ti_3C_2T_x$-rGO electrode illustrates an excellent sensitivity of 0.345 and 0.575 $\mu M \mu A^{-1}$ for Cd^{2+} and Cu^{2+} ions, respectively. $Ti_3C_2T_x$-rGO composite also disclose promising duplicability, repeatability, and consistency of Cd^{2+} and Cu^{2+} detection. Thus, $Ti_3C_2T_x$-rGO is proven as an outstanding electrochemical sensor for identifying Cd^{2+} and Cu^{2+} successfully.

Author Contributions: Conceptualization, R.R.; methodology, D.M., S.F.A.R. and E.M.; software, Y.S.; validation, D.M. and R.R.; formal analysis, D.M.; investigation, D.M.; resources, R.R.; data curation, D.M. and R.R.; writing—original draft preparation, D.M.; writing—review and editing, R.R.; visualization, D.M. and R.R.; supervision, R.R.; project administration, R.R.; funding acquisition, R.R. All authors have read and agreed to the published version of the manuscript.

Funding: This research was funded by the Department of Chemical and Process Engineering, Faculty of Engineering and Built Environment of UKM, Malaysia, Modal Insan Penyelidikan (RGA1) and GUP-2021-027 research grant.

Data Availability Statement: The original contributions presented in this study are included in the article. Further inquiries can be directed to the corresponding author.

Acknowledgments: This work was supported and funded by the Department of Chemical and Process Engineering, Faculty of Engineering and Built Environment of UKM, Malaysia, Modal Insan Penyelidikan (RGA1) and GUP-2021-027 research grant.

Conflicts of Interest: The authors declare no conflict of interest.

References

1. Gumpu, M.B.; Sethuraman, S.; Krishnan, U.M.; Rayappan, J.B.B. A review on detection of heavy metal ions in water–an electrochemical approach. *Sens. Actuators B Chem.* **2015**, *213*, 515–533. [CrossRef]
2. Yin, H.; Zhang, Q.; Zhou, Y.; Ma, Q.; Zhu, L.; Ai, S. Electrochemical behavior of catechol, resorcinol and hydroquinone at graphene-chitosan composite film modified glassy carbon electrode and their simultaneous determination in water samples. *Electrochim. Acta* **2011**, *56*, 2748–2753. [CrossRef]
3. Ahammad, A.J.S.; Rahman, M.M.; Xu, G.-R.; Kim, S.; Lee, J.-J. Highly sensitive and simultaneous determination of hydroquinone and catechol at poly (thionine) modified glassy carbon electrode. *Electrochim. Acta* **2011**, *56*, 5266–5271. [CrossRef]
4. Yi, Y.; Zhao, Y.; Zhang, Z.; Wu, Y.; Zhu, G. Recent developments in electrochemical detection of cadmium. *Trends Environ. Anal. Chem.* **2022**, *33*, e00152. [CrossRef]
5. Shahzad, A.; Rasool, K.; Miran, W.; Nawaz, M.; Jang, J.; Mahmoud, K.A.; Lee, D.S. Two-dimensional $Ti_3C_2T_x$ MXene nanosheets for efficient copper removal from water. *ACS Sustain. Chem. Eng.* **2017**, *5*, 11481–11488. [CrossRef]
6. Yi, Y.; Ma, Y.; Ai, F.; Xia, Y.; Lin, H.; Zhu, G. Novel methodology for anodic stripping voltammetric sensing of heavy-metal ions using Ti 3 C 2 T x nanoribbons. *Chem. Commun.* **2021**, *57*, 7790–7793. [CrossRef]
7. Peng, Q.; Guo, J.; Zhang, Q.; Xiang, J.; Liu, B.; Zhou, A.; Liu, R.; Tian, Y. Unique lead adsorption behavior of activated hydroxyl group in two-dimensional titanium carbide. *J. Am. Chem. Soc.* **2014**, *136*, 4113–4116. [CrossRef]
8. Xia, Y.; Ma, Y.; Wu, Y.; Yi, Y.; Lin, H.; Zhu, G. Free-electrodeposited anodic stripping voltammetry sensing of Cu (II) based on $Ti_3C_2T_x$ MXene/carbon black. *Microchim. Acta* **2021**, *188*, 377. [CrossRef] [PubMed]
9. Xia, Y.; Zhao, Y.; Ai, F.; Yi, Y.; Liu, T.; Lin, H.; Zhu, G. N and P co-doped MXenes nanoribbons for electrodeposition-free stripping analysis of Cu (II) and Hg (II). *J. Hazard. Mater.* **2022**, *425*, 127974. [CrossRef]
10. Maity, A.; Sui, X.; Tarman, C.R.; Pu, H.; Chang, J.; Zhou, G.; Ren, R.; Mao, S.; Chen, J. Pulse-driven capacitive lead ion detection with reduced graphene oxide field-effect transistor integrated with an analyzing device for rapid water quality monitoring. *ACS Sens.* **2017**, *2*, 1653–1661. [CrossRef]
11. Hamsawahini, K.; Sathishkumar, P.; Ahamad, R.; Yusoff, A.R.M. A sensitive, selective and rapid determination of lead (II) ions in real-life samples using an electrochemically reduced graphene oxide-graphite reinforced carbon electrode. *Talanta* **2015**, *144*, 969–976. [CrossRef] [PubMed]
12. Xuan, X.; Hossain, M.; Park, J.Y. A fully integrated and miniaturized heavy-metal-detection sensor based on micro-patterned reduced graphene oxide. *Sci. Rep.* **2016**, *6*, 33125. [CrossRef] [PubMed]
13. Wu, S.; Zhang, K.; Wang, X.; Jia, Y.; Sun, B.; Luo, T.; Meng, F.; Jin, Z.; Lin, D.; Shen, W. Enhanced adsorption of cadmium ions by 3D sulfonated reduced graphene oxide. *Chem. Eng. J.* **2015**, *262*, 1292–1302. [CrossRef]
14. Mohanadas, D.; Azman, N.H.N.; Abdullah, J.; Endot, N.A.; Sulaiman, Y. Bifunctional ternary manganese oxide/vanadium oxide/reduced graphene oxide as electrochromic asymmetric supercapacitor. *Ceram. Int.* **2021**, *47*, 34529–34537. [CrossRef]
15. Mohanadas, D.; Azman, N.H.N.; Sulaiman, Y. A bifunctional asymmetric electrochromic supercapacitor with multicolor property based on nickel oxide/vanadium oxide/reduced graphene oxide. *J. Energy Storage* **2022**, *48*, 103954. [CrossRef]
16. Sengupta, A.; Rao, B.B.; Sharma, N.; Parmar, S.; Chavan, V.; Singh, S.K.; Kale, S.; Ogale, S. Comparative evaluation of MAX, MXene, NanoMAX, and NanoMAX-derived-MXene for microwave absorption and Li ion battery anode applications. *Nanoscale* **2020**, *12*, 8466–8476. [CrossRef]
17. Li, X.; Qian, Y.; Liu, T.; Cao, F.; Zang, Z.; Sun, X.; Sun, S.; Niu, Q.; Wu, J. Enhanced lithium and electron diffusion of $LiFePO_4$ cathode with two-dimensional Ti_3C_2 MXene nanosheets. *J. Mater. Sci.* **2018**, *53*, 11078–11090. [CrossRef]
18. Fang, H.; Pan, Y.; Yin, M.; Pan, C. Enhanced visible light photocatalytic activity of CdS with alkalized Ti_3C_2 nano-sheets as co-catalyst for degradation of rhodamine B. *J. Mater. Sci. Mater. Electron.* **2019**, *30*, 14954–14966. [CrossRef]
19. Mohanadas, D.; Abdah, M.A.A.M.; Azman, N.H.N.; Ravoof, T.B.; Sulaiman, Y. Facile synthesis of PEDOT-rGO/HKUST-1 for high performance symmetrical supercapacitor device. *Sci. Rep.* **2021**, *11*, 11747. [CrossRef]

20. Bai, S.; Shen, X.; Zhong, X.; Liu, Y.; Zhu, G.; Xu, X.; Chen, K. One-pot solvothermal preparation of magnetic reduced graphene oxide-ferrite hybrids for organic dye removal. *Carbon* **2012**, *50*, 2337–2346. [CrossRef]
21. Wang, S.-X.; Maimaiti, H.; Xu, B.; Awati, A.; Zhou, G.-B.; Cui, Y.-D. Synthesis and visible-light photocatalytic N_2/H_2O to ammonia of ZnS nanoparticles supported by petroleum pitch-based graphene oxide. *Appl. Surf. Sci.* **2019**, *493*, 514–524. [CrossRef]
22. Gohari-Bajestani, Z.; Akhlaghi, O.; Yürüm, Y.; Yürüm, A. Synthesis of anatase TiO_2 with exposed (001) facets grown on N-doped reduced graphene oxide for enhanced hydrogen storage. *Int. J. Hydrogen Energy* **2017**, *42*, 6096–6103. [CrossRef]
23. Huang, M.; Yu, J.; Hu, Q.; Su, W.; Fan, M.; Li, B.; Dong, L. Preparation and enhanced photocatalytic activity of carbon nitride/titania (001 vs. 101 facets)/reduced graphene oxide (g-C_3N_4/TiO_2/rGO) hybrids under visible light. *Appl. Surf. Sci.* **2016**, *389*, 1084–1093. [CrossRef]
24. Xu, J.; Liang, Q.; Li, Z.; Osipov, V.Y.; Lin, Y.; Ge, B.; Xu, Q.; Zhu, J.; Bi, H. Rational Synthesis of Solid-State Ultraviolet B Emitting Carbon Dots via Acetic Acid-Promoted Fractions of sp^3 Bonding Strategy. *Adv. Mater.* **2022**, *34*, 2200011. [CrossRef] [PubMed]
25. Chen, Y.; Yang, S.; Zhang, J. The chemical composition and bonding structure of B–C–N–H thin films deposited by reactive magnetron sputtering. *Surf. Interface Anal. Int. J. Devoted Dev. Appl. Tech. Anal. Surf. Interfaces Thin Film.* **2009**, *41*, 865–871. [CrossRef]
26. Mohanadas, D.; Abdah, M.A.A.M.; Azman, N.H.N.; Abdullah, J.; Sulaiman, Y. A promising negative electrode of asymmetric supercapacitor fabricated by incorporating copper-based metal-organic framework and reduced graphene oxide. *Int. J. Hydrogen Energy* **2021**, *46*, 35385–35396. [CrossRef]
27. Rebelo, S.L.; Guedes, A.; Szefczyk, M.E.; Pereira, A.M.; Araújo, J.P.; Freire, C. Progress in the raman spectra analysis of covalently functionalized multiwalled carbon nanotubes: Unraveling disorder in graphitic materials. *Phys. Chem. Chem. Phys.* **2016**, *18*, 12784–12796. [CrossRef]
28. Lorencova, L.; Bertok, T.; Dosekova, E.; Holazova, A.; Paprckova, D.; Vikartovska, A.; Sasinkova, V.; Filip, J.; Kasak, P.; Jerigova, M. Electrochemical performance of $Ti_3C_2T_x$ MXene in aqueous media: Towards ultrasensitive H_2O_2 sensing. *Electrochim. Acta* **2017**, *235*, 471–479. [CrossRef]
29. Yang, Y.-Y.; Zhou, W.-T.; Song, W.-L.; Zhu, Q.-Q.; Xiong, H.-J.; Zhang, Y.; Cheng, S.; Luo, P.-F.; Lu, Y.-W. Terminal Groups-Dependent Near-Field Enhancement Effect of $Ti_3C_2T_x$ Nanosheets. *Nanoscale Res. Lett.* **2021**, *16*, 60. [CrossRef]
30. Genorio, B.; Harrison, K.L.; Connell, J.G.; Dražić, G.; Zavadil, K.R.; Markovic, N.M.; Strmcnik, D. Tuning the selectivity and activity of electrochemical interfaces with defective graphene oxide and reduced graphene oxide. *ACS Appl. Mater. Interfaces* **2019**, *11*, 34517–34525. [CrossRef]
31. Gusain, M.; Nagpal, R. MXene for solar cells. In *Solar Energy Harvesting, Conversion, and Storage*; Elsevier: Amsterdam, The Netherlands, 2023; pp. 171–200.
32. Zhou, Y.; Wang, Y.; Wang, Y.; Li, X. Humidity-enabled ionic conductive trace carbon dioxide sensing of nitrogen-doped $Ti_3C_2T_x$ MXene/polyethyleneimine composite films decorated with reduced graphene oxide nanosheets. *Anal. Chem.* **2020**, *92*, 16033–16042. [CrossRef] [PubMed]
33. Pazniak, A.; Bazhin, P.; Shplis, N.; Kolesnikov, E.; Shchetinin, I.; Komissarov, A.; Polcak, J.; Stolin, A.; Kuznetsov, D. $Ti_3C_2T_x$ MXene characterization produced from SHS-ground Ti_3AlC_2. *Mater. Des.* **2019**, *183*, 108143. [CrossRef]
34. Ta, Q.T.H.; Tran, N.M.; Noh, J.-S. Rice crust-like ZnO/$Ti_3C_2T_x$ MXene hybrid structures for improved photocatalytic activity. *Catalysts* **2020**, *10*, 1140. [CrossRef]
35. Yao, L.; Tian, X.; Cui, X.; Zhao, R.; Xiao, X.; Wang, Y. Partially oxidized $Ti_3C_2T_x$ MXene-sensitive material-based ammonia gas sensor with high-sensing performances for room temperature application. *J. Mater. Sci. Mater. Electron.* **2021**, *32*, 27837–27848. [CrossRef]
36. Ding, X.; Huang, Y.; Li, S.; Zhang, N.; Wang, J. $FeNi_3$ nanoalloy decorated on 3D architecture composite of reduced graphene oxide/molybdenum disulfide giving excellent electromagnetic wave absorption properties. *J. Alloys Compd.* **2016**, *689*, 208–217. [CrossRef]
37. Jin, L.; Chai, L.; Yang, W.; Wang, H.; Zhang, L. Two-dimensional titanium carbides ($Ti_3C_2T_x$) functionalized by poly (m-phenylenediamine) for efficient adsorption and reduction of hexavalent chromium. *Int. J. Environ. Res. Public Health* **2020**, *17*, 167. [CrossRef]
38. Ma, W.; Yao, X.; Sun, D. Simultaneous electrochemical determination of dopamine, epinephrine and uric acid at silver doped poly-l-cysteine film electrode. *Asian J. Chem* **2013**, *25*, 6625–6634. [CrossRef]
39. Mohanadas, D.; Tukimin, N.; Sulaiman, Y. Simultaneous electrochemical detection of hydroquinone and catechol using poly(3,4-ethylenedioxythiophene)/reduced graphene oxide/manganese dioxide. *Synth. Met.* **2019**, *252*, 76–81. [CrossRef]
40. El Hamdouni, Y.; El Hajjaji, S.; Szabó, T.; Trif, L.; Felhősi, I.; Abbi, K.; Labjar, N.; Harmouche, L.; Shaban, A. Biomass valorization of walnut shell into biochar as a resource for electrochemical simultaneous detection of heavy metal ions in water and soil samples: Preparation, characterization, and applications. *Arab. J. Chem.* **2022**, *15*, 104252. [CrossRef]
41. Huang, H.; Chen, T.; Liu, X.; Ma, H. Ultrasensitive and simultaneous detection of heavy metal ions based on three-dimensional graphene-carbon nanotubes hybrid electrode materials. *Anal. Chim. Acta* **2014**, *852*, 45–54. [CrossRef]

42. Tang, Y.-Z.; Gin, K.Y.; Aziz, M. The relationship between pH and heavy metal ion sorption by algal biomass. *Adsorpt. Sci. Technol.* **2003**, *21*, 525–537. [CrossRef]
43. Qu, N.; Zhu, D.; Chan, K.C.; Lei, W. Pulse electrodeposition of nanocrystalline nickel using ultra narrow pulse width and high peak current density. *Surf. Coat. Technol.* **2003**, *168*, 123–128. [CrossRef]
44. Zhu, X.; Liu, B.; Hou, H.; Huang, Z.; Zeinu, K.M.; Huang, L.; Yuan, X.; Guo, D.; Hu, J.; Yang, J. Alkaline intercalation of Ti_3C_2 MXene for simultaneous electrochemical detection of Cd (II), Pb (II), Cu (II) and Hg (II). *Electrochim. Acta* **2017**, *248*, 46–57. [CrossRef]
45. Lv, X.; Pei, F.; Feng, S.; Wu, Y.; Chen, S.-M.; Hao, Q.; Lei, W. Facile synthesis of protonated carbon nitride/$Ti_3C_2T_x$ nanocomposite for simultaneous detection of Pb^{2+} and Cd^{2+}. *J. Electrochem. Soc.* **2020**, *167*, 067509. [CrossRef]
46. Zhang, X.; An, D.; Bi, Z.; Shan, W.; Zhu, B.; Zhou, L.; Yu, L.; Zhang, H.; Xia, S.; Qiu, M. Ti_3C_2-MXene@ N-doped carbon heterostructure-based electrochemical sensor for simultaneous detection of heavy metals. *J. Electroanal. Chem.* **2022**, *911*, 116239. [CrossRef]
47. He, Y.; Ma, L.; Zhou, L.; Liu, G.; Jiang, Y.; Gao, J. Preparation and application of bismuth/MXene nano-composite as electrochemical sensor for heavy metal ions detection. *Nanomaterials* **2020**, *10*, 866. [CrossRef]